Regular article

The association of hydrogen with nanometre bubbles of helium implanted into zirconium

Matthew S. Blackmur [a,*], Simon Dumbill [a], Ian MacLaren [b], David Hernandez-Maldonado [c], Paul D. Styman [a], Mhairi Gass [d], Rebecca J. Nicholls [e], Jonathan M. Hyde [a], Quentin M. Ramasse [c], Kirsty J. Annand [b], James S. Smith [f], Natasha Gotham [f]

[a] National Nuclear Laboratory, Culham Science Centre, Oxfordshire OX14 3DB, United Kingdom
[b] Materials and Condensed Matter Physics, School of Physics and Astronomy, University of Glasgow, Glasgow G12 8QQ, United Kingdom
[c] SuperSTEM Laboratory, SciTech Daresbury Campus, Keckwick Lane, Daresbury WA4 4AD, United Kingdom
[d] Wood plc, Clean Energy Europe, Walton House, Birchwood, WA3 6GA, United Kingdom
[e] The University of Oxford, Department of Materials, Parks Road, Oxford OX1 3PH, United Kingdom
[f] Rolls-Royce plc, PO Box 2000, Derby DE21 7XX, United Kingdom

ABSTRACT

Electron energy-loss spectroscopy (EELS) is used to investigate the association of hydrogen with helium bubbles in zirconium. Conventional EELS data yield a signal at 13.5 eV (similar to the hydrogen K-edge, 13 eV), which is spatially distributed around the peripheries of bubbles and may correlate with the concentration of hydrogen/deuterium in the material. Ultra-high energy resolution EELS yields a signal at 148.6 meV (comparable to a range of Zr—H bonds, 130–156 meV) from a region containing bubbles and no visible hydrides. These signals are interpreted in the context of either bubble surface chemisorption or bubble stress field trapping mechanisms.

Crown Copyright © 2018 Published by Elsevier Ltd on behalf of Acta Materialia Inc. This is an open access article under the Open Government License (OGL) (http://www.nationalarchives.gov.uk/doc/open-government-licence/version/3/).

As an impurity, hydrogen can play a significant role in the degradation and embrittlement of structural metals [1], including steels [2], aluminium [3], titanium [4] and zirconium [5]. Understanding the location and nature of hydrogen in zirconium alloys is important because hydrogen absorbed during aqueous corrosion can lead to property degradation [6] and delayed hydride cracking [7]. Techniques like hot vacuum extraction [8] provide bulk hydrogen measurements, whilst Raman [9], secondary ion-mass [10,11], laser induced plasma spectroscopies [12] and X-ray diffraction [13–15] have sub-micron to millimetre resolutions and can detect hydrogen (or hydrides). However, the majority of potential traps for hydrogen in zirconium are smaller than the resolutions afforded by these techniques and detecting hydrogen on nanometre scales is immensely challenging.

This study addresses this issue by examining the association of hydrogen with nanometre-scale helium bubbles in a zirconium alloy matrix. Literature on iron/steel, aluminium, iron, nickel, copper, molybdenum, palladium and tantalum systems [16–20] suggests that hydrogen can be bound at, or close to, helium bubble surfaces. In those cases, this trapping is thought to occur either through chemisorption [18] or as a product of the stress fields surrounding bubbles [16,21], but no equivalent studies have been performed on zirconium alloys. Aside from bubbles, there are many other potential microstructural traps for hydrogen including vacancies [22], dislocations [23], substitutional species [24] and irradiation-induced matrix defects [25,26], but these are not considered in this paper.

In this work, the association of hydrogen with helium bubbles is explored using Electron Energy-Loss Spectroscopy (EELS). This technique has been successfully used to identify ~50–100 nm diameter hydrogen bubbles formed in biological samples under electron irradiation [27]. Their hydrogen content was confirmed from spectral evidence of the hydrogen K-shell ionisation edge. In inorganic matter, similar evidence for the K-edge has been reported for nano-bubbles both of hydrogen in focused ion beam treated diamond [28] and bubbles in silicon carbide irradiated with H_2^+ and He^+ ions [29]. In both cases, the K-edge signal was taken to indicate the presence of molecular hydrogen.

Recent advances in ultra-high resolution EELS in a new generation of monochromated scanning transmission electron microscopes have enabled vibrational spectroscopy to be performed with nanometre spatial resolutions [30]. As the lightest element, hydrogen yields vibrational peaks of the highest energy, theoretically making it the element most

* Corresponding author at: National Nuclear Laboratory, Building D5, Culham Science Centre, Oxfordshire OX14 3DB, United Kingdom.
E-mail address: matthew.blackmur@alumni.manchester.ac.uk (M.S. Blackmur).

easily detectable using vibrational spectroscopy [31]. However, the spatial resolution of the technique is limited by the delocalised nature of the vibrational features, in that the signal contains a component that is apparent nanometres away from the source [31]. Nonetheless, this technique has been used to detect signals arising from the binding of hydrogen in both titanium hydride and epoxy resin [32].

Zircaloy-4 was studied in 'as-received' and 'deuterium charged' states (charging conditions: 0.1 M KOH and D_2O, 0.1 A·cm^{-2}, 24 h, 20–40 °C). These contained ~10 $_{wt.}$ppm(H) or ~10 $_{wt.}$ppm(H) plus ~120 $_{wt.}$ppm(D), respectively. Approximately 10 $_{wt.}$ppm(H) is intrinsic to manufacturing of Zircaloy-4 and was measured using Hot Vacuum Extraction (HVE). ~120 $_{wt.}$ppm(D) was calculated from weight gain measurements after cathodic charging. Discs with electron transparent regions were prepared by mechanical punching, grinding and electropolishing (5% perchloric acid in methanol, −40 to −60 °C). Electropolishing introduces a small further quantity of hydrogen, which cannot be quantified using HVE because of the low material volume. Henceforth, the two sample conditions are termed 'Low H/D' and 'High H/D', as production of a hydrogen-free sample was unrealistic.

The discs were implanted with 10 keV He^+ ions using the Microscope and Ion Accelerator for Materials Investigations (MIAMI) facility [33]. A beam current of 0.06–0.10 nA (flux of ~2.75×10^{14} to 5×10^{14} ions·cm^{-2}·s^{-1}) achieved 300 nC (fluence of 1.5×10^{18} ions·cm^{-2}). Bubbles were typically ⌀1–7 nm, although some bubbles approaching ⌀10 nm were observed. SRIM [34] calculations indicated helium implantation throughout the thickness of the regions considered suitable for EELS data acquisition. Sample temperatures were maintained at 300 °C during implantations, dissolving ~56 $_{wt.}$ppm of H/D [35] and providing sufficient diffusion mobility for interaction with the forming bubbles.

Samples studied using conventional EELS were first oxygen plasma cleaned. A JEOL ARM-200CF TEM with a Gatan Quantum 965ER electron energy-loss spectrometer was utilised at The University of Glasgow. The instrument was operated at 200 kV and had a Zero-Loss Peak (ZLP) Full-Width at Half-Maximum (FWHM) of ~0.5 eV. The convergence and collection semi-angles were 29 and 36 mrad, respectively.

The High H/D material was studied using Ultra-High-Resolution (UHR) EELS and vibrational spectroscopy, using the Nion UltraSTEM 100 MC 'Hermes' at the SuperSTEM Laboratory [36]. The microscope was operated at 60 kV and had a ZLP FWHM of 0.3 eV, which was improved to 0.02 eV, following monochromation. The convergence and collection semi-angles were 31 and 44 mrad, respectively. Some data were collected using an aloof beam, where delocalised vibrational modes were detected using a beam passing through the vacuum in close proximity to a sample. This effectively removes the spectral background associated with the beam passing through material, thus improving the signal-to-noise ratio.

Analyses were performed using Gatan Digital Micrograph (with additional functionality provided by the EELSTools plugin [37]) and MathWorks Matlab. Zero-loss peak misalignment was calibrated in all data and pixel-to-pixel energy drift (arising from instability in the beam) was corrected for, where necessary. The Principal Component Analysis feature of the Multivariate Statistical Analysis tool [38] was used to remove random noise from conventional EELS data; this tool could not be successfully applied to the UHR EELS data.

Spectral deconvolution analyses were performed using the spectral difference method [39]. This involved subtracting a matrix spectrum from a bubbles spectrum (after scaling to account for thickness differences), yielding the spectral difference. A scaling window of ~45–50 eV was used, encompassing the high energy shoulder of the Zr $N_{2,3}$ edge. Components were identified from the difference spectra, which could be mapped by applying energy-selected windows to the spectrum images. Vibrational modes were extracted from UHR EELS data by subtracting a background function (the sum of two power laws) from the zero-loss peak, yielding difference spectra.

Implanted bubbles are visible as approximately circular regions of darker contrast in Fig. 1a, indicating a reduced material density. Sparse hydrides were also observed at room temperature in the implanted regions (Fig. 1), indicating that for both hydrogen concentrations the bubbles did not suppress hydride formation. The presence of hydrides does not preclude the association of hydrogen with bubbles, as the region of implantation in each electropolished disc is very small, so it would not be sufficient in size to influence the hydrogen concentration in the non-implanted bulk significantly. Consequently, were the bubbles to 'trap' hydrogen at the 300 °C implantation temperature, Fickian diffusion from the non-implanted bulk would ensure the equilibrium solute hydrogen concentration was maintained in the matrix interstices in the implanted region. Upon post-implantation cooling, the non-trapped interstitial hydrogen would then form hydrides in the implanted region as the solubility limit decreased with temperature.

EELS data characteristic of the matrix and bubbles are presented in Fig. 2. The two most prominent signals are the zirconium bulk plasmon oscillation (maximum at 16.6 eV) and the zirconium $N_{2,3}$ shell ionisation edge (reported onset of 29 eV [40], with a delayed maximum observed at 41 eV in the present data). Subtraction of the matrix spectrum from corresponding bubble spectrum yields spectral differences that clearly include the helium K-shell ionisation edge. This feature has a sharp onset reported at 22 eV [41], with an experimentally observed maximum at 23.4 eV, followed by a gradually diminishing tail.

Another signal is apparent to the left of the zirconium bulk plasmon in the spectral difference. This feature is broad, of comparable magnitude to the helium K-edge, has an apparent maximum at 13.5 eV, but appears to be a delayed edge that has an onset around 6 eV. The position of this signal is close to that reported for the hydrogen K-shell ionisation edge (13 eV [42]), but the morphology of this feature differs from that reported elsewhere [28,42]. This may indicate that it arises from, or is superposed upon, signals from another source.

With observed energy ranges for the known helium and possible hydrogen K-shell ionisation edge signals, it becomes possible to map spatially the intensity of these signatures by applying energy-selected windows to the spectrum images. The maps for these energy ranges are given in Fig. 3 for the High H/D and Low H/D samples.

As seen clearly for the High H/D sample (upper in Fig. 3), the feature at 13.5 eV is spatially distributed as rings of intensity around the peripheries of bubbles and will henceforth be referred to as 'halos'. Interestingly, those bubbles mapped from the High H/D sample (upper in Fig. 3) generally appear to possess a stronger halo than those of comparable sizes in the Low H/D sample (lower Fig. 3). This is unlikely to be an artefact of mapping or imaging parameters (such as magnification and resolution), since the pixel sizes are comparable between the maps (0.36×0.36 nm for High H/D versus 0.40×0.40 nm for Low H/D), as are the foil thicknesses (inelastic mean free path range of 0.36–0.66 for High H/D versus 0.42–0.59 for Low H/D). This observation holds true for other datasets not presented here, suggesting that there may be a correlation between hydrogen concentration and halo intensity. However, the present collection of datasets is not sufficiently large to state a robust correlation between hydrogen/deuterium concentration and halo intensity.

If not originating from hydrogen, the observed halos could be cavity (if gaseous bubbles) or interface (if solid bubbles) plasmon oscillations arising from matrix-bubble interfaces [43,44]. David et al. attributed the observation of 12.3–13.3 eV halos around helium nano-bubbles in silicon to originating from cavity plasmon oscillations [45]. However, it is difficult to produce silicon specimens devoid of hydrogen, so those halos observed by David et al. may actually be characteristic of hydrogen associated with the bubbles. Indeed, a later publication by those authors [46] shows a "burst" bubble (containing no helium) that does not have an associated halo. As a burst bubble would still be expected to yield a surface plasmon, its absence suggests that it originates from hydrogen. Although the work of Heyward et al. [20]
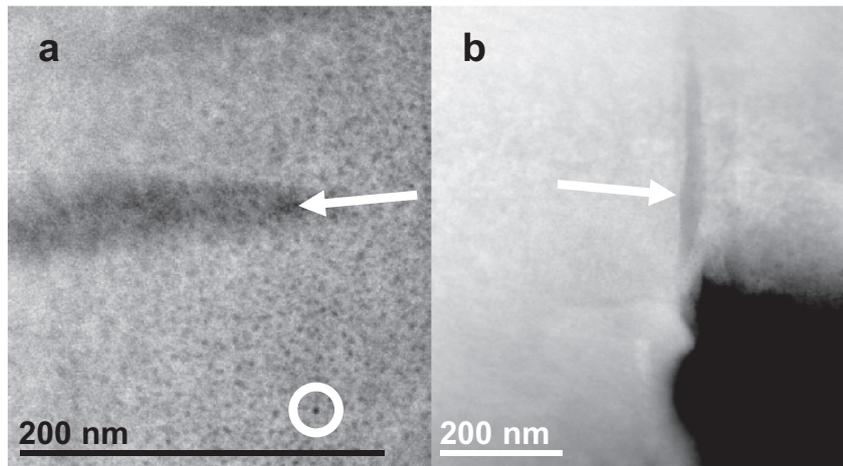
Fig. 1. Annular dark-field images of the bubble implanted regions of the (a) Low H/D and (b) High H/D samples, showing the existence of bubbles (small dark circular contrast, with a circled example) and hydrides (large dark lenticular contrast, examples marked with arrows) at room temperature.

indicates that hydrogen may still associate with the surfaces of empty cavities, this would be at a markedly reduced concentration without the synergistic effect of helium and the excess hydrogen is likely to be released to solution, resulting in a weak or absent halo.

When interpreting the present data within the Drude approximation, a variety of cavity/interface plasmon modes would be excited to a range of intensities at glancing incidence, with calculated plasmon energies ranging over 11.7–13.6 eV. When expanding the approximation to include a sphere of one dielectric material (helium) embedded in a dielectric matrix of another (zirconium), this calculated range blue shifts to 18.2–19.0 eV. From a practical perspective, this indicates that the cavity/interface plasmon of a filled bubble should always exist at a greater energy than that of an empty cavity (which would produce a surface plasmon). This would potentially place any cavity plasmon at a greater energy than the range used to map the observed halos. However, the Drude approximation may not fully describe the dielectric function within the bubble, as this classical treatment includes no description of quantum effects that are likely to be associated with nanometre-sized bubbles. Previous studies on quantum effects have shown red and blue shifts in the plasmon modes of ~0.3–3 eV [47], relative to the classical case, so it appears likely that the ~13.5 eV energy of the observed feature is too low for it to be a plasmon if the bubbles are filled with helium.

To investigate further the possibility that hydrogen is associated with the bubbles, UHR EELS was used to perform vibrational spectroscopy. Spectrum images focused on bubbles yield no strong signals associated with the vibrational modes of hydrogen, likely due to signal attenuation. However, if aloof spectroscopy is performed and spectra are summed from a large region of the vacuum adjacent to material

containing helium bubbles (as in Fig. 4), an inflection is manifest in the tail of the zero-loss peak. When the zero-loss peak tail is background subtracted (using the sum of two power laws), a peak with an apparent maximum at 148.6 meV is observed.

Interestingly, the energy of this feature is comparable to that of the broad vibrational peak associated with solute hydrogen in zirconium (143–144 meV [48,49]) and peaks observed from hydrogen bound in δ—$ZrH_{0.54–1.56}$ (130–140 meV), ε—$ZrH_{1.9–2}$ (136–138 meV and 143–145 meV) and γ—ZrH (141.6–156 meV) [50]. The implication is that the peak in the present data is associated with hydrogen. However, the broad-band nature of the observed signal makes it difficult to interpret as a specific bond and the feature may reflect a range of vibrational modes. These vibrational modes have particularly long ranges (in excess of 100 nm), so although no ZrH_x precipitates are apparent in the survey image in Fig. 4 (suggesting the hydrogen may be associated with the bubbles, which are clearly seen in the vicinity), hydride precipitates cannot be explicitly ruled out as a source.

A model for why hydrogen might be expected to sit in halos around the bubbles is as follows: The propensity for hydrogen to diffuse up a stress gradient towards regions of tension during thermal transients is established in the literature [51]. An internally pressurised bubble is likely to produce compression normal to the bubble surface and tension in the two directions parallel to the bubble surface. Given the state of biaxial tension, local diffusion of hydrogen towards them seems probable, leading to hydrogen enrichment close to the bubble surface [16,17,21]. The balancing hydrogen deficit in the nearby matrix would then be repopulated by hydrogen that diffuses down the concentration gradient from the more remote bulk. Thus, the observed halos may be characteristic of hydrogen associated with surfaces of the bubbles in some way,
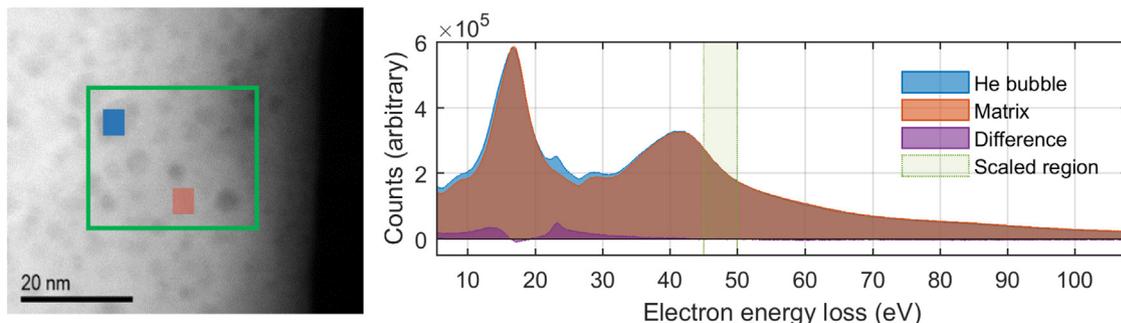
Fig. 2. EELS spectra arising from a helium bubble and the zirconium matrix, scaled to account for thickness differences. The zirconium bulk plasmon oscillation peaks at 16.6 eV, the zirconium $N_{2,3}$-edge peaks at 41 eV and the He K-edge peaks at 23.4 eV.
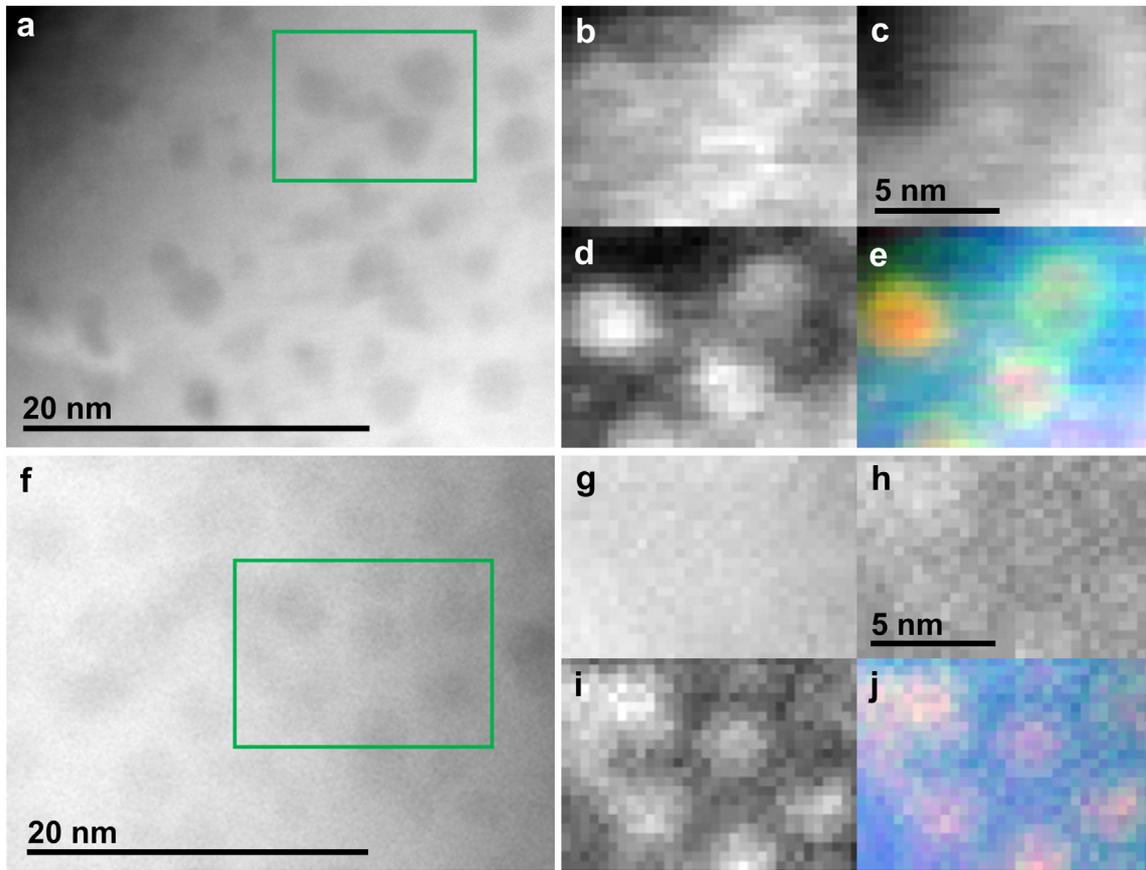
Fig. 3. The spatial distribution of components identified from EELS data acquired from the High H/D (upper) and Low H/D (lower) material conditions. For High H/D, (a) give the annular dark field survey images, (b)-(d) give EELS energy-selected window images (~12–15 eV, ~16.5–19.5 eV and ~22–25 eV), and (e) give a colour composite of these maps. Subplots (f) to (j) follow the same format for Low H/D.

after it has been collected by the tensile stresses. Two alternate mechanisms for this surface binding are described in the literature, either focusing on tensile stress-field trapping [16,21] or a chemisorption-like process [18].

Hydrogen may be trapped close to the bubble-matrix interface by the tensile stresses alone, through modification of the local chemical potential. Such a process is described by Abramov and Eliezer [16,21], giving numerical bases for the aggregation of hydrogen to form halos of enrichment just outside of helium bubbles in iron. Molecular dynamics simulations for tungsten support this hypothesis, indicating hydrogen migrating to the first 1–2 matrix layers outside of the bubbles [19].

Alternatively, chemisorption is suggested by publications describing this behaviour for a number of other metallic matrices containing hydrogen or deuterium. Lee et al. [18] summarise a number of these, contrasting the experimentally determined heat of chemisorption with experimentally and theoretically derived values of hydrogen/deuterium binding enthalpies for helium bubble-associated trap sites. Reasonable agreement was seen for aluminium, iron, nickel, copper, molybdenum and palladium, with a poorer correlation for tantalum being described as a surface contamination effect [18]. Furthermore, density functional theory calculations for helium bubbles in iron indicate that hydrogen consequently forms a shell around the helium
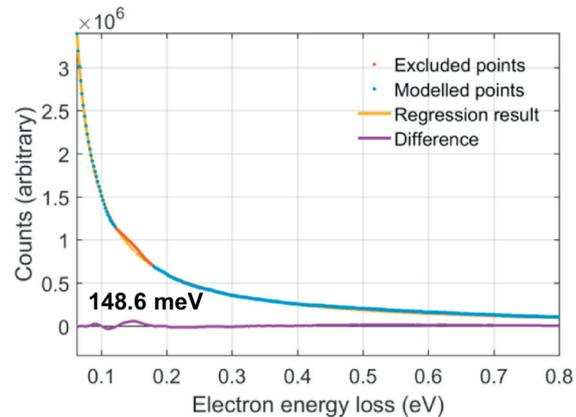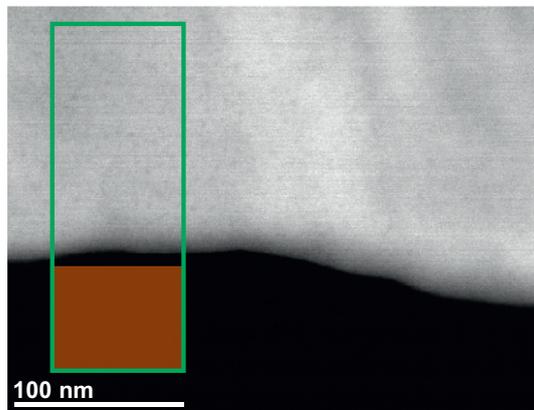
Fig. 4. UHR EELS performed using an aloof beam (sampling only the vacuum, shaded orange) near to a region containing implanted helium bubbles and no visible hydrides.

bubbles, but is attracted and bound to the outer bubble cavity surface [20]. Removal of helium from those simulations retained the hydrogen shell structure around an empty core [20]. Nonetheless, even if a surface chemisorption mechanism dominated, the influence of stress on the chemical potential of solute hydrogen [51] may still allow for an increased quantity of dissolved hydrogen to exist near the bubbles.

In the present dataset, the spectral feature that gives rise to the observed halos exists at a comparable energy to the hydrogen K-ionisation edge. The literature suggests that interstitially solute hydrogen (such as that trapped in a strain field) draws zirconium electrons off the metallic bond and onto the Zr—H bond, which may be covalent-like [52]. This would provide the requisite electron in the K-shell orbital to manifest the associated ionisation edge. Similarly, the literature indicates that the Zr—H bond for a hydride may primarily be covalent [53], so chemisorbed hydrogen may also possess the requisite electron to manifest the K-edge. However, it is noted that the EELS signature for micron-sized hydrides is typically reported in the literature as a characteristic blue shift in the zirconium bulk plasmon [54], rather than manifestation of the K-edge. Lastly, given the EELS signatures for Zr—H bonding [48–50] and the suggested bonding states of hydrogen [52,53], the 148.6 meV signature could be associated with the Zr—H bond for either chemisorbed or stress-trapped (solute) hydrogen, in the absence of hydrides.

It may be possible for hydrogen trapped by either mechanism to manifest bubble halos and both would produce a Zr—H vibrational mode, so these observations do not clearly suggest a specific trapping mechanism. However, these two modes of trapping are not mutually exclusive and the evidence for the attraction of hydrogen to tensile strain fields [51] and the correlation of trap binding enthalpies with heats of chemisorption [18] are both compelling. It may simply be that the strain field attracts and stores a reservoir of solute hydrogen around the bubbles, of which a population becomes chemisorbed.

Overall, these experimental observations provide initial indications in support of the association of hydrogen with bubbles of implanted helium in zirconium. In particular, the nature of the vibrational modes and the possible correlation of sample hydrogen content with the strength of the halos warrant further investigation.

Acknowledgements

References

[1] M.R. Louthan, G.R. Caskey, J.A. Donovan, D.E. Rawl, Mater. Sci. Eng. 10 (1972) 357–368.
[2] R.A. Oriani, Annu. Rev. Mater. Sci. 8 (1) (1978) 327–357.
[3] R. Ambat, E.S. Dwarakadasa, Bull. Mater. Sci. 19 (1) (1996) 103–114.
[4] D.S. Shih, I.M. Robertson, H.K. Bimbaum, Acta Metall. 36 (1) (1988) 111–124.
[5] C.E. Coleman, D. Hardie, J. Less-Common Met. 11 (3) (1966) 168–185.
[6] S.C. Lin, M. Hamasaki, Nucl. Sci. Eng. 71 (3) (1979) 251–266.
[7] P. Adelfang, V. Inozemtsev, IAEA, Vienna, 2010 (ISBN 978-92-0-108610-5)).
[8] Y. Sesha Sayi, K.L. Ramakumar, R. Prasad, C.S. Yadav, P.S. Shankaran, G.C. Chhapru, H.C. Jain, J. Radioanal. Nucl. Chem. 230 (1) (1998) 5–9.
[9] A.K. Kleppe, M. Amboage, A.P. Jephcoa, Sci. Rep. 4 (2014) 4989.
[10] B.F. Kammenzind, D.G. Franklin, H.R. Peters, W.J. Duffin, in: E.R. Bradley, G.P. Sabol (Eds.), Zircon. in the Nucl. Ind.: 11th Int. Symp, ASTM, West Conshohocken 1996, pp. 338–370.
[11] P. Bossis, G. Lelievre, P. Barberis, X. Iltis, F. Lefebvre, in: G.P. Sabol, G.D. Moan (Eds.), Zircon. in the Nucl. Ind.: 12th Int. Symp, ASTM, West Conshohocken 2000, pp. 918–945.
[12] K.H. Kurniawan, T.J. Lie, N. Idris, T. Kobayashi, T. Maruyama, K. Kagawa, M.O. Tjia, A.N. Chumakov, J. Appl. Phys. 96 (2004) 6859–6862.
[13] R.S. Daum, Y.S. Chu, A.T. Motta, J. Nucl. Mater. 392 (3) (2009) 453–463.
[14] M.A. Vicente Alvarez, J.R. Santisteban, G. Domizzi, J. Almer, Acta Mater. 59 (5) (2011) 2210–2220.
[15] M.S. Blackmur, Alloys, The University of Manchester, Manchester, 2015.
[16] E. Abramov, D. Eliezer, J. Mater. Sci. Lett. 7 (1988) 108–110.
[17] W. Hu, L. Guo, J. Chen, F. Luo, T. Li, Y. Ren, J. Suo, F. Yang, Fusion Eng. Des. 89 (2014) 324–328.
[18] S.R. Lee, S.M. Myers, R.G. Spulak, J. Appl. Phys. 66 (1989) 1137.
[19] N. Juslin, B.D. Wirth, J. Nucl. Mater. 438 (2013) S1221–S1223.
[20] E. Hayward, C. Deo, J. Phys. Condens. Matter 24 (2012) 265402.
[21] E. Abramov, D. Eliezer, J. Mater. Sci. 27 (1992) 2595–2598.
[22] M. Christensen, W. Wolf, C. Freeman, E. Wimmer, R.B. Adamson, L. Hallstadius, P.E. Cantonwine, E.V. Mader, J. Nucl. Mater. 460 (2015) 82–96.
[23] B. Cox, J. Alloys Compd. 256 (1–2) (1997) L4–L7.
[24] M. Christensen, W. Wolf, C.M. Freeman, E. Wimmer, R.B. Adamson, L. Hallstadius, P.E. Cantonwine, E.V. Mader, J. Nucl. Mater. 445 (1–3) (2014) 241–250.
[25] M.B. Lewis, J. Nucl. Mater. 125 (1984) 152–159.
[26] B.F. Kammenzind, in: R.J. Comstock, A.T. Motta (Eds.), Zircon. in the Nucl. Ind.: 18th Int. Symp, ASTM, West Conshohocken 2018, pp. 1167–1191.
[27] R.D. Leapman, S. Sun, Ultramicroscopy 59 (1995) 71–79.
[28] W.R. McKenzie, M. Quadir, M.H. Gass, P.R. Munroe, Diam. Relat. Mater. 20 (8) (2011) 1125–1128.
[29] K. Hojou, S. Furuno, K.N. Kushita, N. Sasajima, K. Izui, Nucl. Instrum. Methods Phys. Res., Sect. B 141 (1998) 148–153.
[30] H. Cohen, P. Rez, T. Aoki, P.A. Crozier, N. Dellby, Z. Dellby, D. Gur, T.C. Lovejoy, K. March, M.C. Sarahan, S.G. Wolf, O.L. Krivanek, Microsc. Microanal. 21 (3) (2015) 661–662.
[31] O.L. Krivanek, T.C. Lovejoy, N. Dellby, J. Microsc. 259 (3) (2015) 165–172.
[32] O.L. Krivanek, T.C. Lovejoy, N. Delby, N. Dellby, T. Aoki, R.W. Carpenter, P. Rez, E. Soignard, J. Zhu, P.E. Baston, M.J. Lagos, R.F. Egerton, P.A. Crozier, Nature 514 (2016) 209–212.
[33] J.A. Hinks, J.A. van den Berg, S.E. Donnelly, J. Vac. Sci. Technol. A 29 (2) (2011) 021003.
[34] J.F. Ziegler, M.D. Ziegler, J.P. Biersack, Nucl. Instrum. Methods Phys. Res., Sect. B 268 (11–12) (2010) 1818–1823.
[35] A. McMinn, E.C. Darby, J.S. Schofield, in: G.P. Sabol, G.D. Moan (Eds.), Zircon. in the Nucl. Ind.: 12th Int. Symp, ASTM, West Conshohocken 2000, pp. 173–195.
[36] Q.M. Ramasse, F.S. Hage, D.M. Kepaptsoglou, P. Abellan, J. Yates, R.J. Nicholls, H.C. Nerl, V. Nicolosi, K. Winther, K. Thygesen, P.Z. El Khour, W.P. Hess, F. Azough, R. Freer, Microsc. Microanal. 22 (2016) 964–965.
[37] D.R.G. Mitchell, B. Schaffer, Ultramicroscopy 103 (2005) 319–332.
[38] G. Lucas, P. Burdet, M. Cantoni, C. Hébert, Micron 52–53 (2013) 49–56.
[39] J. Brunley, Philos. Mag. Lett. 66 (1992) 47–56.
[40] [Dataset] Zirconium, Gatan EELS Atlas, http://www.eels.info/atlas/zirconium.
[41] [Dataset] Helium, Gatan EELS Atlas, http://www.eels.info/atlas/helium/.
[42] [Dataset] Hydrogen, Gatan EELS Atlas, http://www.eels.info/atlas/hydrogen/.
[43] M. Natta, Solid State Commun. 7 (1969) 823–825.
[44] P.M. Echenique, A. Howie, D.J. Whealey, Philos. Mag. B 56 (3) (1987) 335–349.
[45] M.-L. David, K. Alix, F. Pailloux, V. Mauchamp, M. Couillard, G.A. Bolton, L. Pizzagalli, J. Appl. Phys. 115 (2014) 123508.
[46] K. Alix, M.L. David, G. Lucas, D.T.L. Alexander, F. Pailloux, C. Hébert, L. Pizzagalli, Micron 77 (2015) 57–65.
[47] C. Colliex, M. Kociak, O. Stéphan, Ultramicroscopy 162 (2016) A1–A24.
[48] R. Hempelmann, D. Richter, B. Stritzker, J. Phys. F: Met. Phys. 12 (1982) 79–86.
[49] R. Khoda-Bakhsh, D.K. Ross, J. Phys. F: Met. Phys. 12 (1982) 15–24.
[50] A.I. Kolesnikov, I.O. Bashkin, A.V. Belushkin, E.G. Ponyatovsky, M. Prager, J. Phys. Condens. Matter 6 (1994) 8989–9000.
[51] B.F. Kammenzind, B.M. Berquist, R. Bajaj, R. Kreyns, D.G. Franklin, in: G.P. Sabol, G.D. Moan (Eds.), Zircon. in the Nucl. Ind.: 12th Int. Symp, ASTM, West Conshohocken 2000, pp. 196–233.
[52] S. Yamanaka, D. Setoyama, H. Muta, M. Uno, M. Kuroda, K. Takeda, T. Matsuda, J. Alloys Compd. 372 (2004) 129–135.
[53] S. Yamanaka, K. Yamada, K. Kurosaki, M. Uno, K. Takeda, H. Anada, T. Matsuda, S. Kobayashi, J. Alloys Compd. 330–332 (2002) 313–317.
[54] K.J. Annand, I. McLaren, M. Gass, J. Nucl. Mater. 465 (2015) 390–399.